analytical chemistry

pubs.acs.org/ac Article

Polarization-Resolved Electrochemiluminescence Sensor Based on the Surface Plasmon Coupling Effect of a Au Nanotriangle-Patterned Structure

Peilin Wang, Junyi Zhao, Zizhun Wang, Zihui Liang, Yixin Nie, Shuping Xu, and Qiang Ma*

Cite This: *Anal. Chem.* 2021, 93, 15785−15793 Read Online

ACCESS | Metrics & More | Article Recommendations | Supporting Information

ABSTRACT: This work focused on the construction of a nanomaterial-patterned structure for high-resolved ECL signal modulation. Due to the surface coupling effect, the different shapes and distribution states of surface plasmonic nanomaterials not only affect the luminescence intensity enhancement but also decide the electrochemiluminescence (ECL) polarization characteristics. Herein, tin disulfide quantum dots were synthesized via a solvothermal method as ECL emitters. Compared with other nanostructures, Au nanotriangle (Au NT) displayed both the localized surface plasmon resonance electromagnetic enhancement effect and the tip amplification effect, which had significant hot spot regions at three sharp tips. Therefore, self-assembled Au NT-based patterned structures with high density and uniform hot spots were constructed as ideal surface plasmonic materials. More importantly, the distribution states of the hot spots affect the polarization characteristics of ECL, resulting in directional ECL emission at different angles. As a result, a polarization-resolved ECL biosensor was designed to detect miRNA 221. Moreover, this polarization-resolved biosensor achieved good quantitative detection in the linear range of 1 fM to 1 nM and showed satisfactory results in the analysis of the triple-negative breast cancer patients' serum.

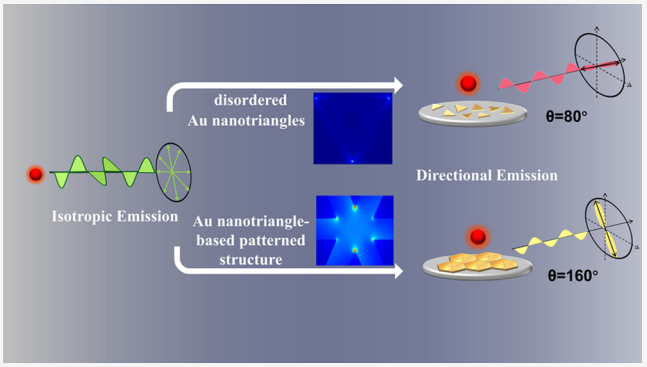

INTRODUCTION

Electrochemiluminescence (ECL) refers to a light-emission process initiated by an electrochemical reaction. Since Si quantum dot (QD) ECL was first reported in 2002, various kinds of nanoparticles with high ECL efficiency have been developed as ECL emitters, such as graphene QDs, MoS_2 QDs, BN QDs, Au nanoclusters (Au NCs), and organic nanoparticles.[1,2] These novel ECL emitters present adjustable spectral characteristics and flexible structural composition compared with traditional tris(2,20-bipyridyl) ruthenium(II) ($Ru(bpy)_3^{2+}$) and luminol. Meanwhile, various ECL-sensing strategies (e.g., ECL-RET,[3] AIE-ECL[4]) have been investigated. ECL technology has shown great potential sensing ability with low background noise and high sensitivity over other methods.[3] Recently, ECL-sensing systems have been developed in tumor marker detection, nucleic acid assay, and visual detection.[5] However, most ECL analyses are still dependent on the total luminescence intensity detection. Despite high sensitivity, highly resolved ECL analysis is an unsolved problem.

In the exploration of ECL-sensing research, surface-enhanced ECL based on the localized surface plasmon resonance (LSPR) of plasmonic materials has been developed. In previous studies, it has been reported that LSPR of Au nanoparticles (Au NPs) can be triggered by ECL emission. Meanwhile, the ECL intensity has been significantly enhanced.[6,7] The surface plasmon oscillation characteristics of noble metal nanoparticles can be adjusted by size, structure, and composition, resulting in a significantly enhanced electromagnetic field. Recently, the surface coupling effect with "hot spots" in luminescence enhancement has attracted the attention of researchers. The anisotropy metallic nanostructures with large specific surface areas and sharp tip positions can provide a significantly stronger electromagnetic intensity, which is called the "hot spot" regions.[8,9] Metal nanoparticles composed of different elements[10] and the gap coupling distance between Au nanoparticle dimers have further been explored for the research of surface plasmon coupling ECL.[11] More importantly, the anisotropic geometry of the noble metal nanostructure allowed for the excitation of hot spots to effectively modulate the polarization properties of the emitted light.[12] For example, periodic spherical nanoparticle arrays coated with a Au layer,[13] vertically ordered gold

Received: September 22, 2021
Accepted: November 4, 2021
Published: November 17, 2021

Scheme 1. (A) Polarization-Resolved ECL of SnS_2 QDs with Disordered Au NTs and a Au NT-Based Patterned Structure and (B) Schematic Illustration of the Polarization-Resolved ECL Biosensor Based on the Au NT-Based Patterned Structure

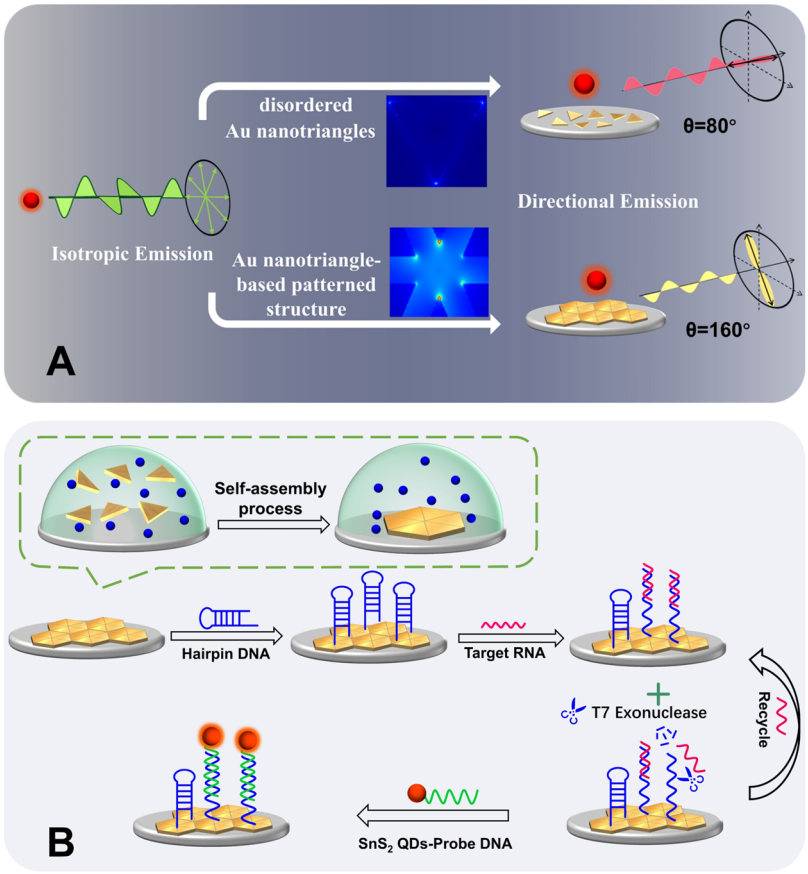

nanorods,[14] and ordered Au nanocone patterned arrays[15] have been used as active substrates for enhanced rapid surface-enhanced Raman scattering (SERS) detection. But most methods for constructing patterned structures at the nanoscale are limited to the traditional etching technique. The operation processes are complicated and inconvenient. Until now, there have been few reports on the patterned nanostructure in surface-enhanced ECL and the impact on ECL polarization characteristics. Therefore, the ordered arrangement and patterning design of plasmonic nanomaterials need to be further explored to construct high-polarization-resolved ECL sensors.

In this work, we developed a polarization-resolved ECL sensor using a self-assembled Au nanotriangle (Au NT)-based patterned structure. The proposed sensor was employed to detect miRNA 221 in the triple-negative breast cancer (TNBC) patient serum samples. The construction process of the ECL biosensor is illustrated in Scheme 1. SnS_2 QDs were synthesized using an ethanol-assisted solvothermal method as ECL emitters. Au NTs were employed as surface plasmonic materials and self-assembled into an ordered hexagonal plane by the process of droplet evaporation driven by depletion force. Au NTs possessed both LSPR electromagnetic enhancement effect and the tip amplification effect. Au NTs had significant hot spot regions at three sharp tips.[16,17] Due to the morphological characteristics, the anisotropic Au NTs had a more sensitive optical response to the change of the surrounding dielectric environment[18] than Au NPs. Furthermore, Au NTs exhibited a tunable wide range of LSPR peaks corresponding to the particle sizes, which can overlap with the ECL spectrum of QDs. Therefore, Au NTs as plasmonic materials had unique advantages to enhance the ECL intensity and tune polarization characteristics of QDs. Furthermore, the patterned structure of the Au NT-based hexagonal plane contributed to the mutual coupling effect of Au NTs and provided uniform hot spots. Therefore, a much stronger enhancement effect and polarization modulation ability for ECL signal in the patterned structure was exhibited. After hairpin DNA was connected with the Au NT-based patterned structure, different concentrations of target miRNA were hybridized with hairpin DNA to open the hairpin loop structure. Then, T7 exonuclease was used to sequentially cut the double-strand structure from 5′ to 3′ and release target miRNA to bind hairpin DNA.[19] Finally, SnS_2 QD-probe DNA completed the hybridization process and resulted in polarization-resolved ECL emission with a Au NT-based patterned structure.

EXPERIMENTAL METHODS

Preparation of SnS_2 QDs and SnS_2 QD-Probe DNA. The process of synthesizing SnS_2 QDs through an ethanol-assisted solvothermal method is summarized as follows. Briefly, 0.021 g of $SnCl_4{\cdot}5H_2O$ and 0.024 g of L-cysteine were dissolved in a mixed solution containing 7 mL of ultrapure water and 3 mL of ethanol. The transparent solution was heated for 30 min at 180 °C in a 1000 W microwave. The yellow product was centrifuged at 10 000 rpm for 10 min. The supernatant was collected and dialyzed. The obtained SnS_2

https://doi.org/10.1021/acs.analchem.1c04120
Anal. Chem. 2021, 93, 15785−15793

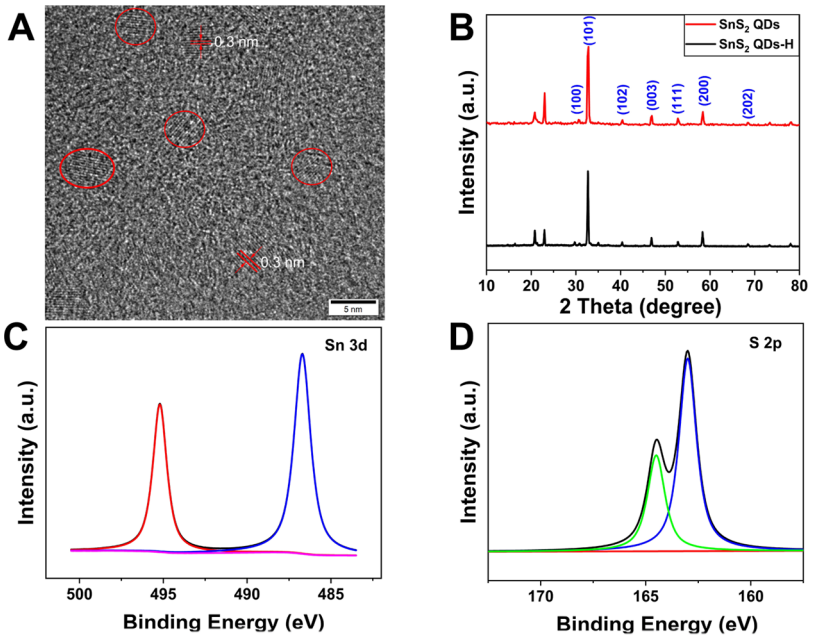

Figure 1. (A) TEM image, (B) XRD pattern, and (C, D) XPS spectra of SnS_2 QDs prepared by the solvothermal method.

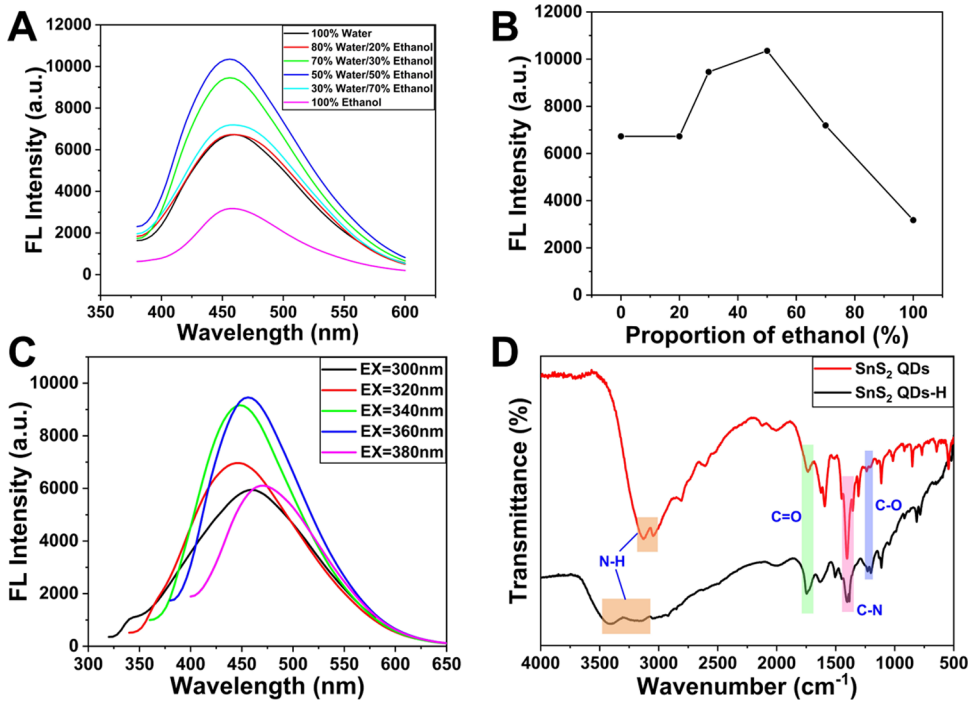

Figure 2. (A) FL intensity of SnS_2 QDs synthesized by different ratios of solvent, (B) curves of the FL intensity variation trend with the proportion of ethanol, and (C) FL emission spectra of SnS_2 QDs at different excitation wavelengths. (D) FTIR spectra of SnS_2 QDs and SnS_2 QDs-H.

QDs were stored at 4 °C for further use. As a control experiment, SnS_2 QDs-H were synthesized with 10 mL of ultrapure water as the solvent using the same procedure. Further, 200 μL of 20 mg/mL EDC and 200 μL of 10 mg/mL NHS mixed solution were added into 2 mL of SnS_2 QDs. Then, 100 μL of 10 μM probe DNA was added and incubated for 2 h to prepare SnS_2 QD-probe DNA. Finally, unreacted DNA in the above solution was removed by dialysis.

Preparation of the Self-Assembled Au NT-Based Patterned Structure. The synthesis procedures of Au NTs are detailed in the Supporting Information. The Au NT dispersion solution was centrifuged and redispersed in equal volumes of different concentrations of CTAC solution as the stock solution. To fabricate Au NT-based patterned structure close-packed structures, 6 μL of each stock solution was dropped on the surface of a glass carbon electrode (GCE) or silicon wafer and fully dried under a lid at room temperature. The environment was kept the same in the drying process of different Au NT stock solutions. The process of droplet evaporation was for about 4 h at room temperature. When self-assembly was achieved, the surface of the substrate presented a metallic luster.

https://doi.org/10.1021/acs.analchem.1c04120
Anal. Chem. 2021, 93, 15785−15793

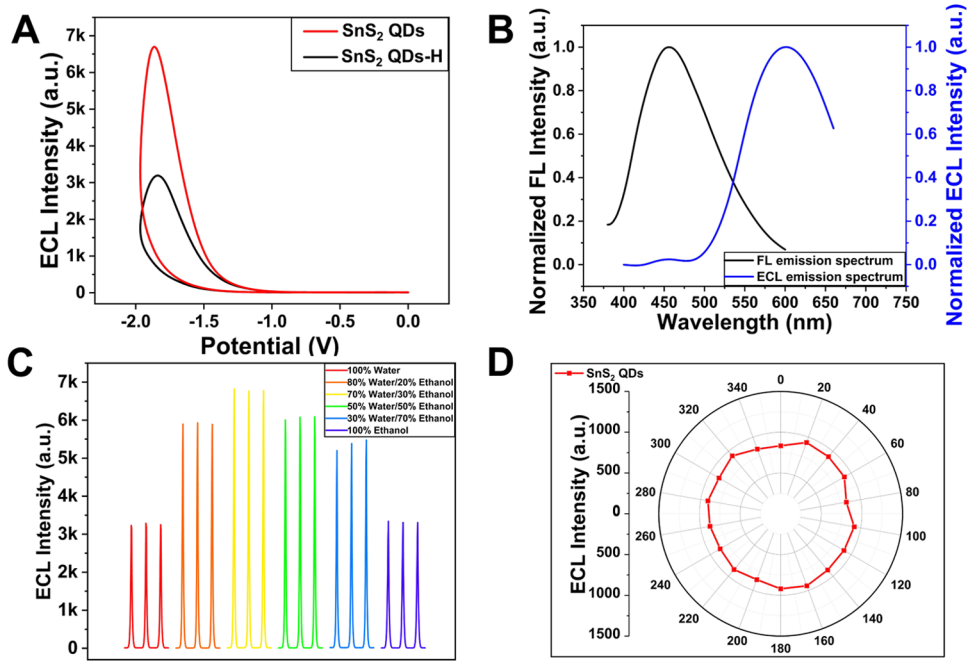

Figure 3. (A) ECL−potential curves of SnS_2 QDs and SnS_2 QDs-H, (B) FL and ECL emission spectra of SnS_2 QDs, (C) ECL intensity of SnS_2 QDs synthesized by different ratios of solvent, and (D) polarization ECL diagram of SnS_2 QDs.

Fabrication of the ECL Biosensor. Hairpin DNA was first annealed at 95 °C for 5 min and cooled to room temperature to form a hairpin structure. Next, 6 μL of 1 μM hairpin DNA was dropped on the surface of the GCE with the self-assembled Au NT-based patterned structure and then incubated at room temperature. After hairpin DNA was successfully connected with Au NTs via Au−S bonds, 6 μL of different concentrations of miRNA 221 were added. The hybridization process was completed at 37 °C in 2 h. Next, 50 U/mL T7 exonuclease was dropped and incubated for 2 h to achieve the recycling process. Finally, 4 μL of SnS_2 QD-probe DNA solution was added and incubated at 37 °C for 2 h. Unreacted regents were washed away in the measurement process. All of the ECL tests were performed in 10 mM phosphate-buffered saline (PBS, pH 7.4) containing 50 mM potassium persulfate ($K_2S_2O_8$) as the co-reactant. The ECL signal was recorded in the co-reactant under cyclic voltammetry from −2 to 0 V. Finally, miRNA 221 in the TNBC patient serum from China-Japan Union Hospital of Jilin University was detected. The electrochemical data and ECL signals were obtained using an ECL20 electroluminescent instrument from Guangzhou Ingsens Sensor Technology Co. Ltd.

RESULTS AND DISCUSSION

Characterization of SnS_2 QDs. The high-resolution TEM (HRTEM) image in Figure 1A exhibits the morphological characteristics of SnS_2 QDs. SnS_2 QDs were uniformly dispersed with an average size of 5 nm. The HRTEM image also clearly showed that the lattice fringe spacing of SnS_2 QDs was 0.3 nm. The crystal phase of SnS_2 QDs was investigated utilizing X-ray diffraction (XRD). Figure 1B shows the contrast pattern of SnS_2 QDs prepared by the solvothermal method and the hydrothermal method. The main diffraction peak positions matched with the crystal planes of the hexagonal SnS_2 structure.[20] There were no obvious differences between the patterns. This indicated that the crystal morphologies of SnS_2 QDs were similar. X-ray photoelectron spectroscopy (XPS) was used to analyze the elemental composition and the valence states of SnS_2 QDs. As shown in Figure 2C, the two peaks located at 486.7 and 495.2 eV were, respectively, attributed to Sn $3d_{5/2}$ and Sn $3d_{3/2}$, which confirmed the existence of Sn^{4+}. Figure 2D exhibits the S 2p spectrum, which was the feature of S^{2-}. The binding energies peaks at 486.7 and 495.2 eV were attributed to S $2p_{3/2}$ and S $2p_{1/2}$, respectively. The S 2p and Sn 3d spectra of SnS_2 QDs prepared by the hydrothermal method are displayed in Figure S1. The two peaks of 487.2 and 495.9 eV were assigned to Sn $3d_{5/2}$ and Sn $3d_{3/2}$ of Sn^{4+}, respectively. The peaks at 163.3 and 165.0 eV were attributed to S $2p_{3/2}$ and S $2p_{1/2}$, respectively. For comparison, the binding energy of Sn and S elements in SnS_2 QDs prepared with the solvothermal method demonstrated a lower value. The results demonstrated the presence of sulfur vacancies[21,22] in SnS_2 QDs.

To explore the solvent work in the preparation of SnS_2 QDs, a series of SnS_2 QDs were synthesized with different volume ratios of water and ethanol. The fluorescence emission intensities changed with the variation of the solvent composition. QDs grew more uniformly in the mixed solvent containing water and ethanol. Meanwhile, the mixed solvent can change the oxidation state of the SnS_2 atomic layers of QDs.[23,24] The separation efficiency of photoexcited electron−hole pairs benefited from the existence of the oxidation products.[25] As a result, the fluorescence intensity of SnS_2 QDs showed a gradual enhancement as the proportion of ethanol increased. When the ratio of ethanol in the solvent was 50%, the fluorescence intensity reached the maximum. SnS_2 QDs synthesized with ethanol as the solvent had obvious fluorescence quenching. The fluorescence quenching was attributed to the lower solubility of sulfur source compounds in ethanol and the reduced reaction activity. Figure 2B shows that SnS_2 QDs had excitation wavelength-dependent characteristics. The fluorescence emission peaks showed a red shift as the excitation wavelength increased. UV−vis absorption spectra are recorded in Figure S2. Both SnS_2 QDs and SnS_2

https://doi.org/10.1021/acs.analchem.1c04120
Anal. Chem. 2021, 93, 15785−15793

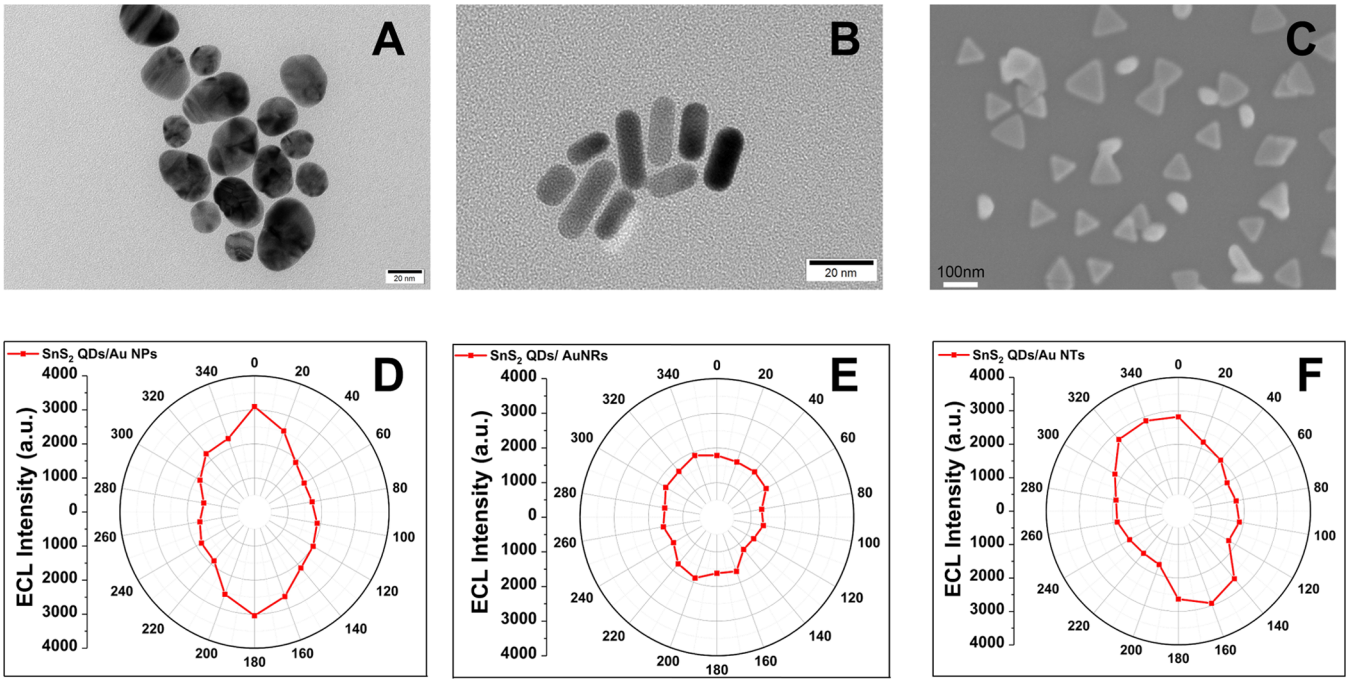

Figure 4. (A) TEM image of Au NPs, (B) TEM image of Au NRs, and (C) SEM image of Au NTs. Polarization ECL diagram of SnS_2 QDs with (D) Au NPs, (E) Au NRs, and (F) Au NTs.

QDs-H displayed absorption bands at 272 nm. The functional groups on the surface of SnS_2 QDs were investigated using Fourier transform infrared (FTIR) spectroscopy in Figure 2D. The double peaks at around 3200 cm^{-1} were attributed to the stretching vibration of N−H, and the peaks at wavenumbers 1600−1640 cm^{-1} corresponded to the bending vibration of N−H. The results indicated the presence of the amino group. Moreover, the peaks at 1735 and 1407 cm^{-1}, respectively, corresponded to C═O and C−N.[20,26]

ECL Behavior of SnS_2 QDs. The SnS_2 QDs generated strong ECL emission under the same testing conditions from −2 to 0 V in PBS (pH 7.4) containing 50 mM $K_2S_2O_8$. The ECL−potential curves in Figure 3A showed that the excitation potential of SnS_2 QDs was at −1.80 V. In addition, the cyclic voltammetry (CV) curves in Figure S3 showed that the reduction peaks of SnS_2 QDs and SnS_2 QDs-H were at −1.12 and −1.21 V, respectively. The lower voltage illustrated that the SnS_2 QDs synthesized by the solvothermal method can be reduced more easily in the ECL process. As a result, more excited-state QDs* emerged, triggering ECL emission enhancement. The ECL mechanism of SnS_2 QDs can be illustrated by the following equations.

$$SnS_2QDs + e^- \rightarrow SnS_2QDs^{-\cdot} \quad (1)$$

$$S_2O_8^{2-} + e^- \rightarrow SO_4^{-\cdot} + SO_4^{2-} \quad (2)$$

$$SO_4^{-\cdot} + SnS_2QDs^{-\cdot} \rightarrow SnS_2QDs^* + SO_4^{2-} \quad (3)$$

$$SnS_2QDs^* \rightarrow SnS_2QDs + h\nu \quad (4)$$

The ECL emission spectrum and the FL emission spectrum of SnS_2 QDs are demonstrated in Figure 3B. The ECL and FL emission peak of SnS_2 QDs was located at 600 and 455 nm, respectively. The observed 45 nm red shift of the ECL emission spectrum was attributed to the different luminescence mechanisms of QDs. The ECL and FL of QDs originated from surface state and intrinsic emission, respectively.[27] Different solvents in the synthesis process also played an important role in the ECL intensity of SnS_2 QDs. Figure 3C demonstrates the trend of the ECL intensity of SnS_2 QDs that were prepared using different ratios of water and ethanol. The ethanol-assisted solvothermal synthesis method resulted in the generation of vacancies of QDs. The ECL intensity of SnS_2 QDs was enhanced when ethanol was added to the reaction precursor solution. When the volume ratio of ethanol was 30%, the ECL intensity of SnS_2 QDs was the maximum, which was two times stronger than that of SnS_2 QDs-H. In accordance with the variation trend of fluorescence intensity, the ECL intensity decreased constantly after increasing the volume of ethanol. This was related to the electrostatic interaction between the vacancies and carriers,[28] which sped up the electron transfer and obtained highly efficient electron−hole recombination.[29] Meanwhile, the SnS_2 QDs in Figure S3B displayed excellent ECL stability. With 50 mM $K_2S_2O_8$, the ECL signal remained constant in continuous electrochemical reaction cycles (more than 10 times). Therefore, the SnS_2 QDs synthesized with the ethanol-assisted solvothermal method were used in the following experiment. To show the ECL features of SnS_2 QDs, the ECL signal was detected with the angle of the polarizer from 0 to 330°. The result in Figure 3D indicated that the ECL emission of SnS_2 QDs was isotropic.

Polarization-Resolved ECL with Different Au Nanostructures. The electromagnetic field coupling between the emission of QDs and the metallic plasmon material appears at different polarization angles under different surface charge distributions.[30] Therefore, the isotropic ECL emission of QDs can be amplified and converted into the directional emission in the presence of metal plasmons.[10] Figure 4 demonstrates the effect on the ECL polarization characteristics of SnS_2 QDs with three different Au nanomaterials, including Au NPs, Au NRs, and Au NTs. These Au nanomaterials possessed different shapes and ECL enhancement abilities. When Au NPs with an average particle size of about 30 nm and Au NTs with a side

https://doi.org/10.1021/acs.analchem.1c04120
Anal. Chem. 2021, 93, 15785−15793

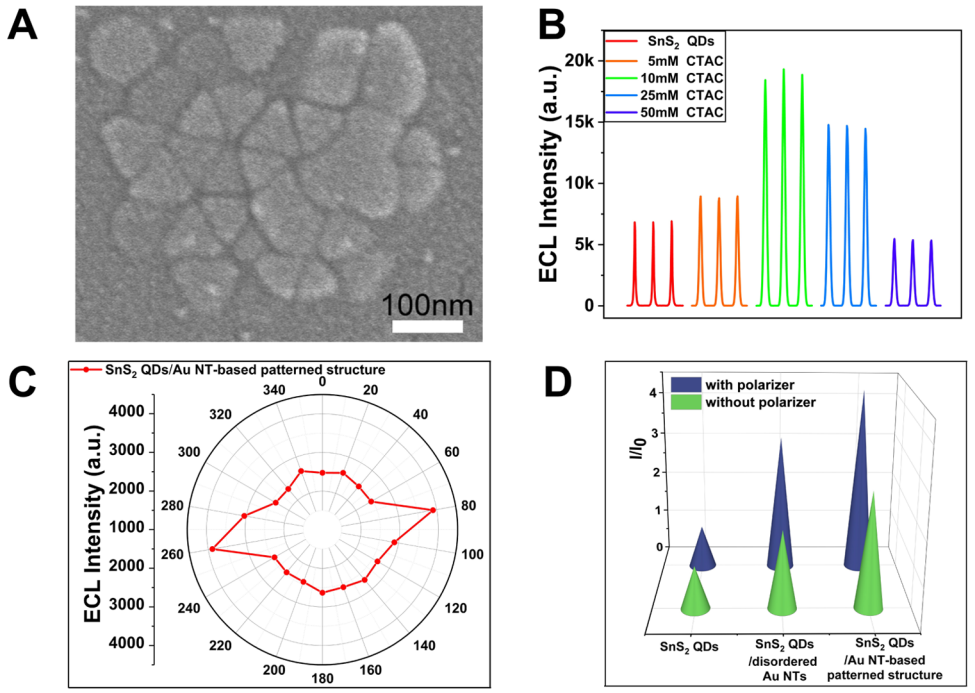

Figure 5. (A) SEM image of the Au NT-based patterned structure, (B) ECL intensity of SnS_2 QDs with Au NTs dispersed in different concentrations of CTAC, (C) polarization ECL diagram of the SnS_2 QDs/Au NT-based patterned structure, (D) ECL enhancement factor of SnS_2 QDs, SnS_2 QDs/dispersed Au NTs, and SnS_2 QDs/Au NT-based patterned structure with or without a polarizer.

length of around 100 nm were used as plasmonic materials, polarization at the orientation angle was observed. The surface plasmon bands of Au NPs and Au NTs were located at 530 and 670 nm (Figure S4), respectively, which overlapped with the ECL emission of SnS_2 QDs at 600 nm to generate the isotropic surface coupling effect. The different extinction spectra of Au NPs and Au NTs caused the inconsistent resonance effect with the ECL emission at a fixed wavelength of SnS_2 QDs, resulting in different polarization angles (θ = 0, 180 and 160, 340°, respectively). Therefore, the ECL intensity of SnS_2 QDs increased to 3.5 and 3.3 times, respectively, under the polarization angle. With Au NRs (25 nm length, 8 nm diameter), the ECL of SnS_2 QDs can be enhanced 2.0 times. There was no obvious polarized ECL in the SnS_2 QDs with Au NRs. This was due to the electron oscillation of Au NRs in both the transverse and longitudinal axes of the rod on account of the shape characteristics.[31] The orientation of disorderly Au NRs was random, which lead to the simultaneous generation of surface plasmon coupling in the two axes. The disturbance between the mutual coupling of different parts further resulted in the uneven distribution of the electromagnetic field intensity.[32]

The ECL enhancement largely depended on the localized electric field distribution of the plasmon material. Au NTs with three sharp tips efficiently realized the concentration of light and the enhancement of the localized electric field. The strong hot spots generated by Au NTs greatly improved the surface enhancement efficiency. Therefore, Au NTs were further used to construct orderly structures to obtain the strong and uniformly distributed hot spot regions. The self-assembly process of the Au NT-based patterned structure is illustrated in Scheme 1B. When Au NT solution with CTAC molecule as the depletant was placed on the GCE, the depletion force was generated. Depletion attraction was the adjustable driving force to achieve the self-assembly process. When the Au NTs were close to each other, the depletants were excluded from the space between the nanoparticles. The local concentration gradient of CTAC pushed the Au NTs together.[33,34] During the solvent drying process, the depletion attraction strength gradually increased with the concentration of droplets, resulting in close-packed self-assembled structures in varying degrees on the substrate.[35] The concentration of CTAC in the dispersed solution system was from 5 to 50 mM. Different concentrations of CTAC can generate strong or weak depletion forces during the self-assembly process, which caused the excessive aggregation or dispersion structural morphology of Au NTs (Figure S5). Figure 5A displays the SEM image of the Au NT-based patterned structure with 10 mM CTAC solution. The ECL intensity of SnS_2 QDs on the Au NT-based patterned structure had a 2.8-fold enhancement. This indicated that 10 mM CTAC was the optimal concentration in obtaining the self-assembled structure. When the concentration of CTAC reached 50 mM, the ECL intensity was decreased. The chaotic stacking form of Au NTs, displayed in Figure S5C, indicated that the irregular LSPR effect and high concentration of micelles covering the Au NT surface hindered the ECL generation process. Compared with dispersed Au NTs, the ECL polarization angle range became narrower with high resolution (Figure 5C). The ECL generated from the SnS_2 QDs/Au NT-based patterned structure also exhibited the characteristics of polarization at the directional angle (θ = 80, 260°). In the self-assembled Au NT coupled regions, these equilateral triangles were close to each other to form a compact plane. The self-assembled Au NT-based patterned structure provided a strong surface coupling effect at the tips and gap regions of the triangles, which resulted in the uniform hot spot distribution. As shown in Figure 5D, the different extents of ECL intensity enhancement were recorded. The polarization-resolved ECL intensity of SnS_2 QDs displayed 3.3- and 4.3 times enhance-

https://doi.org/10.1021/acs.analchem.1c04120
Anal. Chem. 2021, 93, 15785−15793

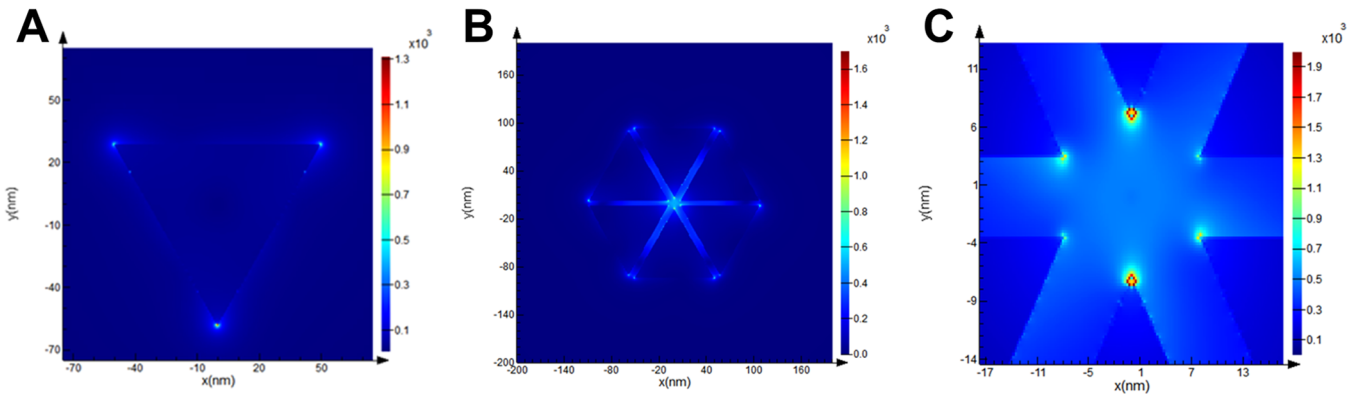

Figure 6. FTDT simulation of electromagnetic field intensity distributions of (A) Au NT and (B) the Au NT-based patterned structure. (C) Partially enlarged FTDT simulation of electromagnetic field intensity of the Au NT-based patterned structure.

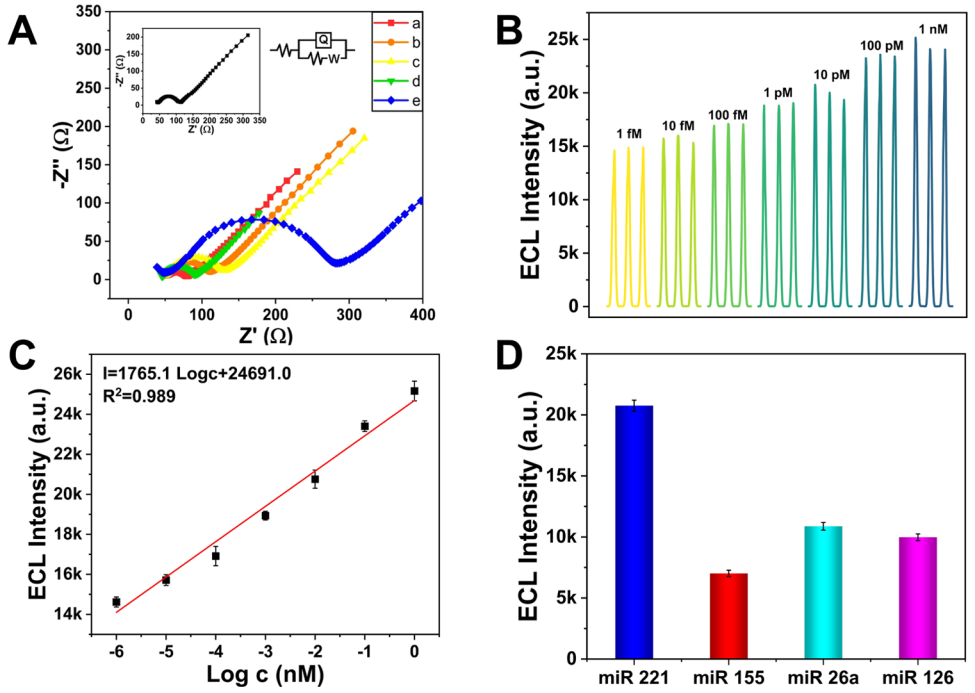

Figure 7. (A) EIS results of (a) the Au NT-based patterned structure, (b) a connected with hairpin DNA, (c) b connected with target RNA, (d) c treated with T7 exonuclease, and (e) d connected with SnS_2 QDs-probe DNA. The inset graph depicts the EIS results of the electrode. (B) Relationship between the ECL intensity and different concentrations of miRNA 221. (C) Corresponding linear relationship for miRNA 221 detection. (D) Selectivity test with miRNA 221, miRNA 155, miRNA 26a, and miRNA 126.

ment with the dispersed Au NTs and the patterned structure, respectively. The electromagnetic field distribution of single Au NT and Au NT-based patterned structure nanostructures is demonstrated by finite-difference time-domain (FDTD) simulations in Figure 6. The FTDT simulations were calculated under the 600 nm incident light using commercial software (Lumerical Solutions, Inc.), and the type of the incident source applied in this modulation was dipole circularly polarized light. The electromagnetic field is most effectively amplified at the tip of the Au NT due to its sharp features. The Au NT-based patterned structure nanostructures displayed a stronger electromagnetic field enhancement in Figure 6B. Hot spots were densely distributed at the coupling regions of the edges, especially at the vertex position (Figure 6C). The strong electromagnetic field distribution in this region led to the significant ECL enhancement.

Analytical Performance of the Polarization-Resolved Biosensor. The construction process of the entire polarization-resolved biosensor was characterized step by step using electrochemical impedance spectroscopy (EIS). The semicircle diameter of the Nyquist diagram evaluated the charge transfer resistance of the electrode interface. As shown in Figure 7A, when the hairpin DNA was successfully connected with the Au NT-based patterned structure through Au−S bonds, the impedance increased from 79.3 to 110.6 Ω. The value of impedance increased to 130.6 Ω when target miRNA was hybridized with hairpin DNA to open the hairpin loop structure. After T7 exonuclease was added to cut the double-stranded hybrid part, the impedance was reduced to 91.6 Ω. Finally, when SnS_2 QDs and probe DNA were connected, the impedance greatly increased to 282.6 Ω. The changing process of the impedance value confirmed the successful establishment of this sensing system. Different concentrations of miRNA 221

https://doi.org/10.1021/acs.analchem.1c04120
Anal. Chem. 2021, 93, 15785−15793

were detected to evaluate the analytical performance of this biosensor. As the concentration of miRNA increased, the ECL intensity increased. The linear relationship between ECL intensity and the logarithmic of miRNA concentration is recorded in Figure 7C, fitted as $I = 1765.1 \log c + 24\,691.0$ ($R^2 = 0.989$). The detection of limit was calculated at 0.71 fM (LOD = $3\sigma/S$), where σ represents the standard deviation of blank signals and S is to the slope of the calibration plot. In addition, other types of miRNA (miRNA 155, miRNA 26a, and miRNA 126) were employed to evaluate the anti-interference ability of this biosensor. The results in Figure 7D demonstrated that this biosensor produced a selective response to miRNA 221 at the same concentration. The results indicated that this sensing strategy had good polarization-resolved ability in the detection of miRNA 221. The previously reported methods for the determination of miRNA 221 are listed in Table S2. Compared with other reports, this polarization-resolved ECL method exhibited a wide linear range and low detection limit. Figure S6A displays the stability of the detection method. The intra- and interassay assessments were also investigated in Figure S6B. The results indicated that this ECL biosensor had acceptable reproducibility (RSD ≤ 3.67%). Serum samples of TNBC patients and healthy persons were also tested. As shown in Table 1, the standard addition method was used to investigate the analytical performance of this biosensor in these actual samples. The recovery rates were in the range of 93 and 110%. The above results indicated that the increased expression level of miRNA 221 was a potential feature of TNBC and related to pathogenesis.

Table 1. Detection of miRNA 221 in Human Serum Samples

sample	detected	added	found	recovery (%)
TNBC patient 1		10.0 fM	9.80 fM	98
TNBC patient 2	0.60 pM	0.60 pM	1.25 pM	108
TNBC patient 3		1.00 pM	0.93 pM	93
TNBC patient 4		100.0 pM	107.0 pM	107
healthy person 1		100.0 pM	110.0 pM	110
healthy person 2		0.10 pM	0.095 pM	95

CONCLUSIONS

In this work, we constructed a polarization-resolved ECL biosensor based on the Au NT-based patterned structure to detect miRNA 221. The solvothermal method was used to improve the electrochemical reaction activity of SnS_2 QDs. Different metallic nanomaterials with various shapes and distributions were investigated. The self-assembled Au NT-based patterned structure had a high density and uniform hot spots. As a result, the ECL intensity of QDs was amplified. Moreover, the Au NT-based patterned structure can modulate the ECL polarization characteristics of QDs. Therefore, the polarization-resolved ECL biosensor has been designed to detect miRNA 221 in the actual sample. For the development of polarization-resolved ECL research in the future, the relationship between the morphologies of metal nanostructures and the polarization luminescence characters should be further explored.

ASSOCIATED CONTENT

Supporting Information

The Supporting Information is available free of charge at https://pubs.acs.org/doi/10.1021/acs.analchem.1c04120.

Chemicals and apparatus; synthesis of Au NPs, Au NRs, and Au NTs; XPS images of SnS_2 QDs and SnS_2 QDs-H (Figure S1); UV−vis spectra of SnS_2 QDs and SnS_2 QDs-H (Figure S2); curves of the ECL intensity variation trend with the proportion of ethanol (Figure S3); CV curves of SnS_2 QDs and SnS_2 QDs-H in PBS (pH 7.4) containing 50 mM $K_2S_2O_8$ (Figure S3); ECL stability of SnS_2 QDs (Figure S3); UV−vis spectra of Au NPs, Au NRs, and Au NTs (Figure S4); SEM images of Au NTs assembled in different concentrations of CTAC (Figure S5); stability of the ECL biosensor (Figure S6); repeatability of the ECL biosensor (Figure S6); names and sequences of all of the oligonucleotides used in this work (Table S1); and comparison of other methods with this work (Table S2) The use of human serum samples has been approved by the ethics committee of the China-Japan Union Hospital of Jilin University (No. 2021-KYLY-020016). (PDF)

AUTHOR INFORMATION

Corresponding Author

Qiang Ma − *Department of Analytical Chemistry, College of Chemistry, Jilin University, Changchun 130012, China;* orcid.org/0000-0003-4841-5005; Email: qma@jlu.edu.cn

Authors

Peilin Wang − *Department of Analytical Chemistry, College of Chemistry, Jilin University, Changchun 130012, China*

Junyi Zhao − *State Key Laboratory of Supramolecular Structure and Materials, College of Chemistry and Institute of Theoretical Chemistry, College of Chemistry, Jilin University, Changchun 130012, China*

Zizhun Wang − *Electron Microscopy Center, Jilin University, Changchun 130012, China*

Zihui Liang − *Department of Analytical Chemistry, College of Chemistry, Jilin University, Changchun 130012, China*

Yixin Nie − *Department of Analytical Chemistry, College of Chemistry, Jilin University, Changchun 130012, China;* orcid.org/0000-0002-8560-4131

Shuping Xu − *State Key Laboratory of Supramolecular Structure and Materials, College of Chemistry and Institute of Theoretical Chemistry, College of Chemistry, Jilin University, Changchun 130012, China;* orcid.org/0000-0002-6216-6175

Complete contact information is available at: https://pubs.acs.org/10.1021/acs.analchem.1c04120

Notes

The authors declare no competing financial interest.

ACKNOWLEDGMENTS

The present work was supported by the National Natural Science Foundation of China (No. 22174051), the science research project (No. JJKH20211050KJ) in the Education Department of Jilin Province, China, and the Graduate Innovation Fund of Jilin University.

REFERENCES

(1) Liang, Z. H.; Zhang, Q.; Nie, Y. X.; Zhang, X.; Ma, Q. *Anal. Chem.* **2020**, *92*, 9223−9229.

(2) Nie, Y. X.; Zhang, X.; Zhang, Q.; Liang, Z. H.; Ma, Q.; Su, X. G. *Biosens Bioelectron.* **2020**, *160*, No. 112217.

(3) Lu, H. J.; Xu, J. J.; Zhou, H.; Chen, H. Y. *TrAC, Trends Anal. Chem.* **2020**, *122*, No. 115746.
(4) Wei, X.; Zhu, M. J.; Cheng, Z.; Lee, M.; Yan, H.; Lu, C.; Xu, J. J. *Angew. Chem., Int. Ed.* **2019**, *58*, 3162−3166.
(5) Fu, Y.; Ma, Q. *Nanoscale* **2020**, *12*, 13879−13898.
(6) Shan, Y.; Xu, J. J.; Chen, H. Y. *Chem. Commun.* **2009**, 905−907.
(7) Wang, J.; Shan, Y.; Zhao, W. W.; Xu, J. J.; Chen, H. Y. *Anal. Chem.* **2011**, *83*, 4004−4011.
(8) Kohout, C.; Santi, C.; Polito, L. *Int. J. Mol. Sci.* **2018**, *19*, 3385.
(9) Gao, Y.; Wang, J.; Wang, W.; Zhao, T.; Cui, Y.; Liu, P.; Xu, S.; Luo, X. *Anal. Chem.* **2021**, *93*, 2480−2489.
(10) Liang, Z. H.; Nie, Y. X.; Zhang, X.; Wang, P. L.; Ma, Q. *Anal. Chem.* **2021**, *93*, 7491−7498.
(11) Zhang, Q.; Tian, Y.; Liang, Z. H.; Wang, Z. Z.; Xu, S. P.; Ma, Q. *Anal. Chem.* **2021**, *93*, 3308−3314.
(12) Lee, H.; Kim, G. H.; Lee, J. H.; Kim, N. H.; Nam, J. M.; Suh, Y. D. *Nano Lett.* **2015**, *15*, 4628−4636.
(13) Zhang, H. H.; Zhou, F.; Liu, M.; Liu, D. L.; Men, D. D.; Cai, W. P.; Duan, G. T.; Li, Y. *Adv. Mater. Interfaces* **2015**, *2*, No. 1500031.
(14) Martín, A.; Wang, J. J.; Iacopino, D. *RSC Adv.* **2014**, *4*, 20038−20043.
(15) Liu, D. M.; Wang, Q. K.; Hu, J. *Appl. Surf. Sci.* **2015**, *356*, 364−369.
(16) Otsuki, J.; Sugawa, K.; Jin, S. *Mater. Adv.* **2021**, *2*, 32−46.
(17) Ni, Y.; Kan, C. X.; Xu, J.; Liu, Y. *Superlattices Microstruct.* **2018**, *114*, 124−142.
(18) Kelly, K. L.; Coronado, E.; Zhao, L. L.; Schatz, G. C. *J. Phys. Chem. B* **2003**, *107*, 668−677.
(19) Wang, M.; Fu, Z. L.; Li, B. C.; Zhou, Y. L.; Yin, H. S.; Ai, S. Y. *Anal. Chem.* **2014**, *86*, 5606−5610.
(20) Srivastava, R. R.; Mishra, H.; Singh, V. K.; Vikram, K.; Srivastava, R. K.; Srivastava, S. K.; Srivastava, A. *J. Lumin.* **2019**, *213*, 401−408.
(21) Cao, H. W.; Bai, Z.; Li, Y. T.; Xiao, Z. R.; Zhang, X. W.; Li, G. Z. *ACS Sustainable Chem. Eng.* **2020**, *8*, 7343−7352.
(22) Wang, J. B.; Huang, J. J.; Huang, S. P.; Notohara, H.; Urita, K.; Moriguchi, I.; Wei, M. D. *ACS Sustainable Chem. Eng.* **2020**, *8*, 9519−9525.
(23) Zhang, B.; Liu, C.-y.; Liu, Y. *Eur. J. Inorg. Chem.* **2010**, *2010*, 4411−4414.
(24) Ding, H.; Ji, Y.; Wei, J. S.; Gao, Q. Y.; Zhou, Z. Y.; Xiong, H. M. *J. Mater. Chem. B* **2017**, *5*, 5272−5277.
(25) Jiao, X. C.; Li, X. D.; Jin, X. Y.; Sun, Y. F.; Xu, J. Q.; Liang, L.; Ju, H. X.; Zhu, J. F.; Pan, Y.; Yan, W. S.; Lin, Y.; Xie, Y. *J. Am. Chem. Soc.* **2017**, *139*, 18044−18051.
(26) Srivastava, R. R.; Singh, V. K.; Srivastava, A. *Opt. Mater.* **2020**, *109*, No. 110337.
(27) Sun, M. F.; Liu, J. L.; Zhou, Y.; Zhang, J. Q.; Chai, Y. Q.; Li, Z. H.; Yuan, R. *Anal. Chem.* **2020**, *92*, 14723−14729.
(28) He, Y. P.; Hou, S. F.; Yang, L. Q.; Zhang, F.; Zou, G. Z. *Chem. − Eur. J.* **2018**, *24*, 9592−9597.
(29) Wang, F.; Lin, J.; Zhao, T. B.; Hu, D. D.; Wu, T.; Liu, Y. *J. Am. Chem. Soc.* **2016**, *138*, 7718−7724.
(30) Mertens, H.; Biteen, J. S.; Atwater, H. A.; Polman, A. *Nano Lett.* **2006**, *6*, 2622−2625.
(31) Mehere, A.; Chaure, N. B. *Appl. Phys. A.* **2020**, *126*, No. 662.
(32) Xin, H. P.; Liu, F.; Ren, G. J.; Zhao, H. L.; Yao, J. Q. *Opt. Commun.* **2017**, *389*, 92−96.
(33) Young, K. L.; Jones, M. R.; Zhang, J.; Macfarlane, R. J.; Esquivel-Sirvent, R.; Nap, R. J.; Wu, J.; Schatz, G. C.; Lee, B.; Mirkin, C. A. *Proc. Natl. Acad. Sci. USA* **2012**, *109*, 2240−2245.
(34) Zhang, J.; Lang, P. R.; Meyer, M.; Dhont, J. K. *Langmuir* **2013**, *29*, 4679−4687.
(35) Kim, J.; Song, X. H.; Ji, F.; Luo, B. B.; Ice, N. F.; Liu, Q. P.; Zhang, Q.; Chen, Q. *Nano Lett.* **2017**, *17*, 3270−3275.

https://doi.org/10.1021/acs.analchem.1c04120
Anal. Chem. 2021, 93, 15785−15793